iScience

CellPress
OPEN ACCESS

Article

Diameter-dependent assessment of microvascular leakage following ultrasound-mediated blood-brain barrier opening

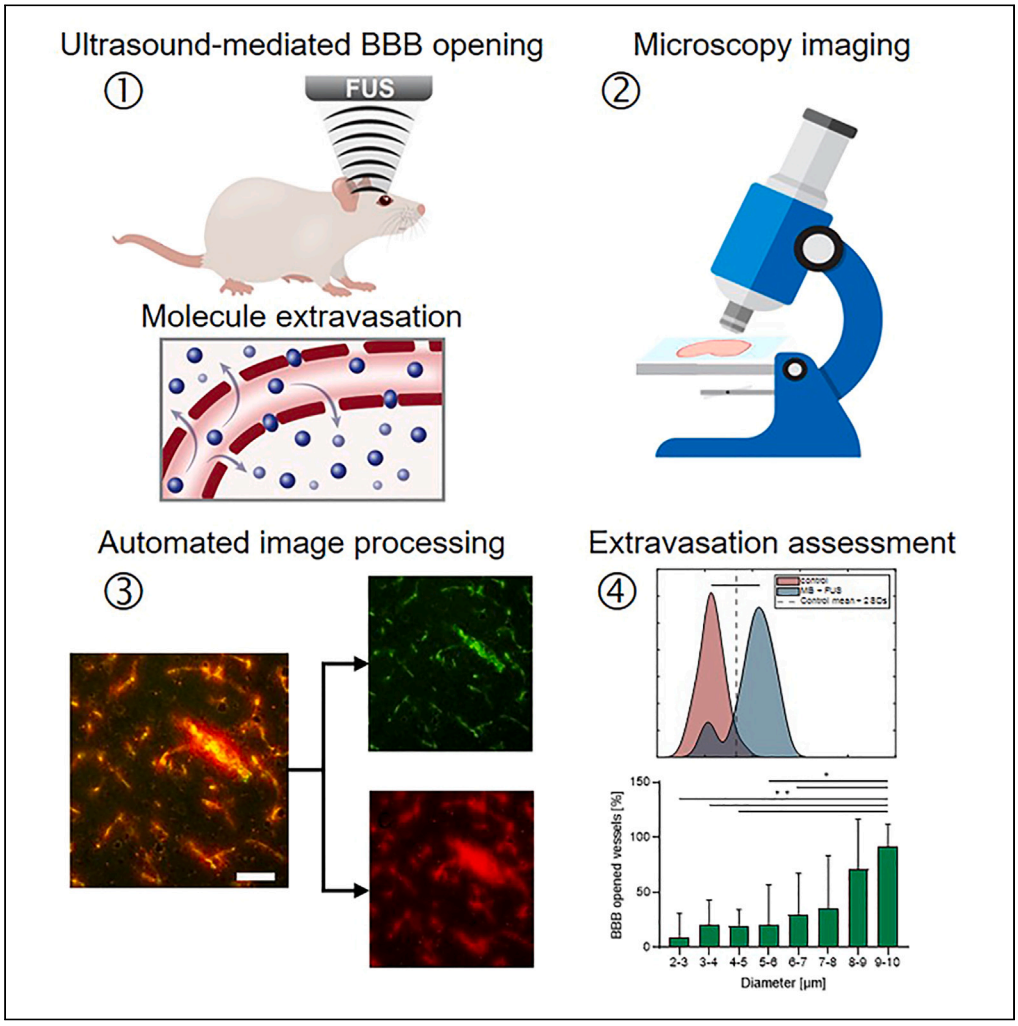

Sharon Katz, Roni Gattegno, Lea Peko, Romario Zarik, Yulie Hagani, Tali Ilovitsh

ilovitsh@tauex.tau.ac.il

Highlights

We present a method to quantify BBB opening as a function of vessel diameter

High resolution of 1 µm for vessels with a diameter <10 µm is achieved

The high resolution enables to explore drug delivery to the brain from capillaries

Our findings demonstrate that BBB opening depends on capillary diameter

Katz et al., iScience 26, 106965
June 16, 2023
https://doi.org/10.1016/j.isci.2023.106965

iScience

CellPress
OPEN ACCESS

Article

Diameter-dependent assessment of microvascular leakage following ultrasound-mediated blood-brain barrier opening

Sharon Katz,[1,2] Roni Gattegno,[2] Lea Peko,[1] Romario Zarik,[1,2] Yulie Hagani,[1,2] and Tali Ilovitsh[1,2,3,*]

SUMMARY

Blood brain barrier disruption (BBBD) using focused ultrasound (FUS) and microbubbles (MB) is an effective tool for therapeutic delivery to the brain. BBBD depends to a great extent on MB oscillations. Because the brain vasculature is heterogenic in diameter, reduced MB oscillations in smaller blood vessels, together with a lower number of MBs in capillaries, can lead to variations in BBBD. Therefore, evaluating the impact of microvasculature diameter on BBBD is of great importance. We present a method to characterize molecules extravasation following FUS-mediated BBBD, at a single blood vessel resolution. Evans blue (EB) leakage was used as marker for BBBD, whereas blood vessels localization was done using FITC labeled Dextran. Automated image processing pipeline was developed to quantify the extent of extravasation as function of microvasculature diameter, including a wide range of vascular morphological parameters. Variations in MB vibrational response were observed in blood vessel mimicking fibers with varied diameters. Higher peak negative pressures (PNP) were required to initiate stable cavitation in fibers with smaller diameters. *In vivo* in the treated brains, EB extravasation increased as a function of blood vessel diameter. The percentage of strong BBBD blood vessels increased from 9.75% for 2–3 μm blood vessels to 91.67% for 9–10 μm. Using this method, it is possible to conduct a diameter-dependent analysis that measures vascular leakage resulting from FUS-mediated BBBD at a single blood vessel resolution.

INTRODUCTION

Safe, transient and localized blood-brain barrier disruption (BBBD) is essential for therapeutic delivery to the brain for a variety of brain diseases, becausethe BBB creates an obstacle to effective drug delivery.[1] The BBB is a unique formation that selectively restricts substance exchanges between the circulatory system and the brain parenchyma. The BBB plays a significant role in preventing pathogenic contamination of the brain; however, it also poses serious limitations on neurological treatment as it prevents most drugs from reaching the brain.[2] The BBB normally excludes drugs that measure 0.4 kDa or more. In recent years, focused ultrasound (FUS) has emerged as a noninvasive therapeutic approach that enables the treatment of the brain at low frequencies (below 650 kHz) that can penetrate an intact human skull.[3,4] FUS-mediated thermal ablation has been used to treat over 500 patients for brain indications including brain tumors, essential tremor, psychiatric applications, chronic pain, and epilepsy.[1] When low-energy ultrasound (US) is combined with intravenously (IV) injected microbubbles (MBs); i.e., efficient theranostic probes that concurrently serve as contrast agents and therapeutic agents, the BBB opens in a noninvasive and localized manner,[5] thus enabling drug delivery via a variety of mechanisms, including transport through cells and through gap junctions to cross from the bloodstream to the brain.[6] Currently, FUS-mediated BBBD clinical trials are ongoing for a variety of brain diseases.[5,7,8]

FUS-mediated BBBD is tightly linked to MB oscillations. Stable cavitation occurs when the MBs undergo repeated cycles of expansion and contraction under relatively low peak negative pressures (PNP). In these conditions, an MB that is present within a blood vessel exerts mechanical forces on the surrounding endothelial cells that increases their permeability and allows substances to perfuse into the parenchyma.[6] When the PNP is increased, the MB oscillates in inertial cavitation, which may be destructive to the surrounding

[1]Department of Biomedical Engineering, Tel Aviv University, Tel Aviv, Israel

[2]The Sagol School of Neuroscience, Tel Aviv University, Tel Aviv, Israel

[3]Lead contact

*Correspondence: ilovitsh@tauex.tau.ac.il

https://doi.org/10.1016/j.isci.2023.106965

tissue.[9,10] Therefore, safe BBBD requires careful selection of the PNP to maintain the MBs in stable cavitation. *In situ*, MB cavitation can be monitored in real time by passive cavitation detection (PCD), which makes it possible to identify specific signatures in the MB echo spectra that are associated with stable vs. inertial cavitation.[11,12] For this reason, it is often used as live feedback for safe FUS-mediated BBBD.[13] More recent developments include the stable cavitation dose (SCD) and inertial cavitation dose (ICD) which are used as advanced metrics for evaluating the MB vibrational response during FUS treatment.[14]

MB oscillations depend on many parameters such as their formulation,[15] size[16] and concentration.[17] Another major parameter is the applied US frequency. For the low frequency range employed for BBBD (around 250 kHz), MB oscillations are significantly enhanced.[18–23] Therefore, there is a narrow range of PNPs that can be implemented for safe BBB.[24] One key aspect that impacts MBs oscillations is the physiological structure of the blood vessels. The brains of mammals and other species are composed of a dense vascular network that facilitates the supply of nutrients and oxygen required for brain metabolism.[25,26] This network is inherently heterogenic in diameter, although small capillaries dominate in all brain regions.[27] Conversely, the blood vessels in the brain continuously undergo short and long-term changes in diameter.[28] The effective distribution of drugs within the brain is likely to require homogeneous openings in large and small blood vessels. However, MBs oscillations were shown to be constrained when the MBs are contained within vessel-mimicking rigid-walled tubes, and in *ex vivo* capillaries with highly compliant wall.[29–32] This is commonly attributed to interactions between the MB and the vessel wall, because of the MB large diameter (1.5–4 μm). Further, in super-resolution (SR) US imaging of the brain microvasculature, the acquisition time was reported to be significantly increased in capillaries as a result of the limited MB access and slower blood flow.[31] Because both MB oscillations and concentration play a key role in the success of BBBD, and because the brain vasculature is inherently heterogenic in diameter,[27] reduced MB oscillations in smaller blood vessels, together with the lower MB concentration in capillaries can lead to variations in BBBD, which are likely to interfere with therapeutic outcomes. Therefore, a method that could assess variations in BBBD as a function of blood vessel diameter is greatly needed.

Fluorescent molecules extravasation following FUS-mediated BBBD opening has been observed previously at a single blood vessel resolution using *in vivo* two-photon fluorescence microscopy (2PFM) in mice.[33–36] Although this method provides high spatiotemporal resolution, it has various limitations. First, *in vivo* 2PFM is limited by the laser penetration depth mainly to superficial regions such as the cerebral cortex, however, in many cases, FUS-mediated BBBD is applied to deeper brain regions. Furthermore, in 2PFM there is a tradeoff between spatial resolution, sensitivity, and acquisition time. As a result, the field of view generally covers only a small fraction of the brain, where the total amount of blood vessels observed simultaneously is on the order of tens of vessels. Finally, to enlarge the field of view, most *in vivo* 2PFM studies minimize scan duration via a reduction of spatial resolution. Consequently, most studies focus on blood vessels with diameters above 10 μm, and include very few vessels with smaller diameters. Because the majority of the blood vessels in the mouse brains are smaller than 10 μm,[37,38] if variations in BBBD exist in these vessels, they are likely to have a major effect. However, because of these limitations, little is known about variations in small capillaries following FUS-mediated BBBD, and in different regions of the brain. In this paper we developed a robust, high resolution and large-scale method for fluorescent molecules extravasation assessment across the BBB after FUS-mediated BBBD at a single blood vessel resolution, to identify variations as a function of blood vessel diameter. Our approach provides a high resolution of <1 μm that can detect differences between vessels with a diameter of less than 10 μm, where large variations in BBB extravasation were observed. In addition, it can detect variations in BBBD in all of the brain regions.

The US parameters control the extent of the BBBD, which dictates the size of the delivered molecules. Typical molecules are a few nanometers in size,[8] such as Evans blue (EB), fluorescent dyes that are conjugated to larger molecules such as albumin or Dextran or magnetic resonance imaging contrast agents; however, larger molecules such as antibodies, genes and stem cells can also be delivered.[39] The molecular weight (MW) of the conjugated Dextran determines the extent of dye penetration into the parenchyma following BBBD.[40] Our method utilizes two fluorescent dyes. The staining is observed *ex vivo* in different regions of the dissected brain, with submicronic resolution. Subsequent to FUS-mediated BBBD, mice were co-injected with two dyes: a large 2000 kDa FITC-Dextran that remained in the blood stream following BBBD, and EB, which is one of the most frequently used BBB impermeable dyes for BBB leakage observation. Its advantage lies in the fact that it appears blue in the visible spectrum, but also fluoresces in red, which facilitates the identification of the treated area under microscopy. EB penetrates into the

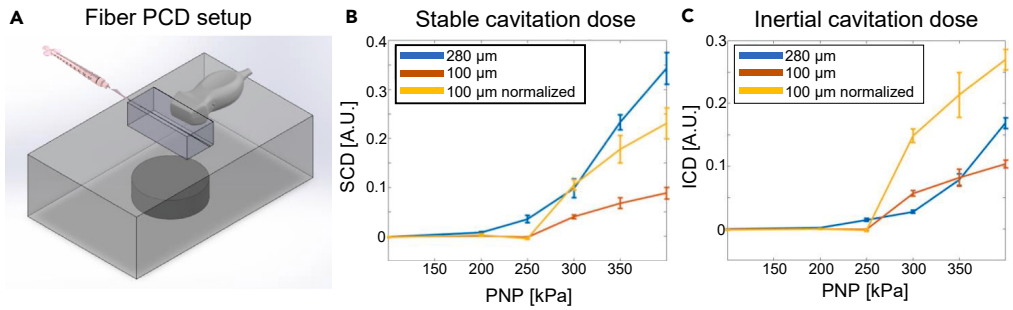

Figure 1. Passive cavitation detection in blood vessel mimicking tubes

(A) A 250 kHz single element transducer was used to insonify tissue-mimicking phantom embedding tubes of either 280 or 100 µm containing an MB suspension. PCD was performed with an array transducer located perpendicularly to the therapeutic transducer. The acoustic echoes were processed, yielding results as a function of the applied PNP and the different tube diameters. (B) SCD, and (C) ICD.

(B and C) 280 µm and 100 µm results are depicted by the blue and orange lines, respectively. The yellow line represents the results of the 100 µm capillary when multiplied by the cross-section ratio. All data are plotted as mean ± SD.

parenchyma following BBBD, and can be found in the blood stream as long as 24 h following systemic administration.[41] FITC-Dextran was used for morphological evaluation of the blood vessels, whereas the EB was used to localize the source of the BBBD within single blood vessels, and for the evaluation of the extent of extravasation to the parenchyma around each vessel. This approach was previously used for quantifying BBB leakage after chemically induced BBBD.[40,42] Here, we describe a robust platform for evaluating the effects of microvasculature diameter on BBBD.

RESULTS

Passive cavitation detection

MB oscillations were evaluated in blood vessel mimicking tubes via PCD, to identify variations as a function of tube diameter. PCD was performed with an imaging array (ATL P4-1, Philips, WA, USA), during MBs interaction with a therapeutic pulse at a center frequency of 250 kHz (Figure 1A). The SCD and ICD were computed based on the recorded radiofrequency (RF) echoes.[14] Both SCD and ICD increased as a function of the applied PNP; however, the onset of the SCD increase occurred at a PNP of 200 kPa for the larger tube with a diameter of 280 µm, and a PNP of 250 kPa for the smaller 100 µm tube (both for the raw data and the normalized data based on MB volume within the tube) (Figure 1B). The onset of ICD shifted similarly to the SCD; however, the increase slope was steeper for the 100 µm normalized fiber (Figure 1C). This suggests that there was a sharp transition between stable and inertial cavitation for MBs in smaller tubes.

In-vivo experiments

BBB extravasation as a function of blood vessel diameter was assessed *in vivo*. Mice underwent BBBD using MB and 250 kHz US. Subsequently, two fluorescent dyes were systemically injected: 2000 kDa FITC-Dextran that fluoresces in green and stains the blood vessels, and EB that fluoresces in red and serves to evaluate the BBB extravasation. In the first set of experiments, the brain preservation and microscopy imaging techniques were optimized to determine the brain slice thickness, microscope parameters and the dye circulation duration before brain harvesting. The optimized parameters were then used to quantify BBBD.

Optimization experiments

Two brain preservation methods were tested on control mice (no BBB-opening), either using standard paraformaldehyde (PFA) fixation or flash-freezing using liquid-nitrogen (Figure 2). After PFA fixation, there was FITC-Dextran leakage from the blood vessels that made it impossible to localize the blood vessels (Figure 2A). In comparison, blood vessels were easily identified in the green channel using the flash-freezing technique which was hence selected for the subsequent experiments. The next step was to choose the slice thickness using the control brains. The 12 µm slices yielded blurry images with heterogeneous coloring within the blood vessels, whereas the 50 µm slices were blurry because of out-of-focus blood vessels beyond the depth of field. The 20 µm slices yielded the highest quality images, with a clear view of the blood vessels, and an overlap between the green and red channels (Figures 2B–2D).

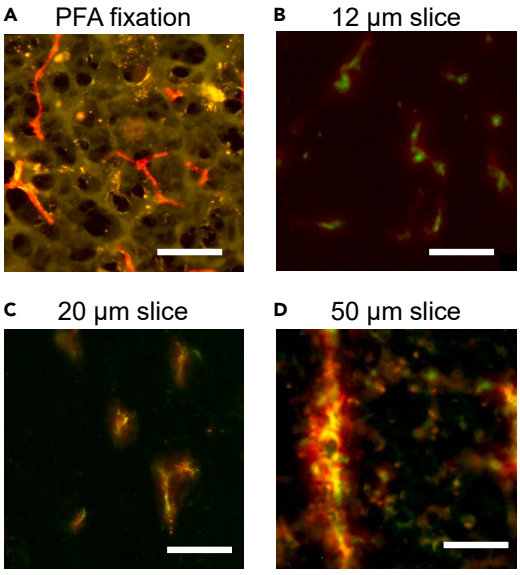

Figure 2. Brain preservation and slice thickness optimization of the control brains

Microscopy images of (A) PFA fixed brain, and flash frozen brains with slice thickness of (B) 12 µm. (C) 20 µm. (D) 50 µm. Scale bars are 50 µm.

Next, BBBD was performed using a custom setup (illustrated in Figure 3A). Standard EB leakage following BBBD resulted in blue stains that were visible in the brain (Figure 3B). However, these strong stains implied broad extravasation and perfusion of the EB within the brain tissue that prevented blood vessel localization. Here, to enable BBBD detection at the resolution of a single blood vessel, mild EB leakage was required (Figure 3C). Fluorescent images of the EB leakage pattern can also be used to optimize EB extravasation (Figures 3D–3G). Differences in the amount of extravasation were achieved by adapting the EB circulation duration. This setp was done to identify a duration that was long enough to allow EB perfusion into the parenchyma following BBBD, while avoiding widespread diffusion that would make the leakage source undetectable (Figure S1). The FITC-Dextran circulation duration was 10 min, based on previous studies.[42] This duration was selected as a tradeoff between effective vascular staining and minimized possible BBB penetration, because larger molecules require a longer circulation time to extravasate from the blood stream. The sonication pressure was chosen such that no signs of microhemorrhage were observed during histology (PNP of 263 kPa).

Single-blood vessel-based BBB opening quantification

Microscopy images of brain slices following BBBD with US and MBs showed reliable blood vessel staining (green) and widespread extravasation of EB (red) around the blood vessels compared to the control brains. In the control brains, the EB was confined to the blood vessels and thus overlapped with the green channel (Figure 4A). In the treated brains, EB extravasation increased with applied PNP, whereas variations in EB intensity around each blood vessel were visible (Figures 4B–4D).

Quantification of the amount of EB extravasation was carried out by an automated image processing algorithm developed for this task, which is further discussed in the STAR Methods section (Figure 5). Briefly, the original image was split into two channels. The green channel was used for vessel segmentation and morphological feature extraction (Figures 5B and 5C). The red channel was used to quantify EB intensity around each blood vessel (Figure 5D). The median pixel intensity of the normalized red channel was calculated in the region of interest (ROI), and chosen according to the processing of the green channel. Extravasation was then analyzed for each blood vessel individually, resulting in a detailed quantification of a range of parameters, including blood vessel diameter distribution, blood vessel length and bifurcation density for each brain region, amount of EB extravasation as a function of blood vessel diameter, and the fraction of strong BBB opened blood vessels.

The image processing algorithm was initially applied to both the control and the treated datasets to compute the microvasculature diameter distribution within the regions where the BBB was opened. The average microvasculature diameter was 4.98 $\pm$ 1.9 µm and was similar in the control and treated

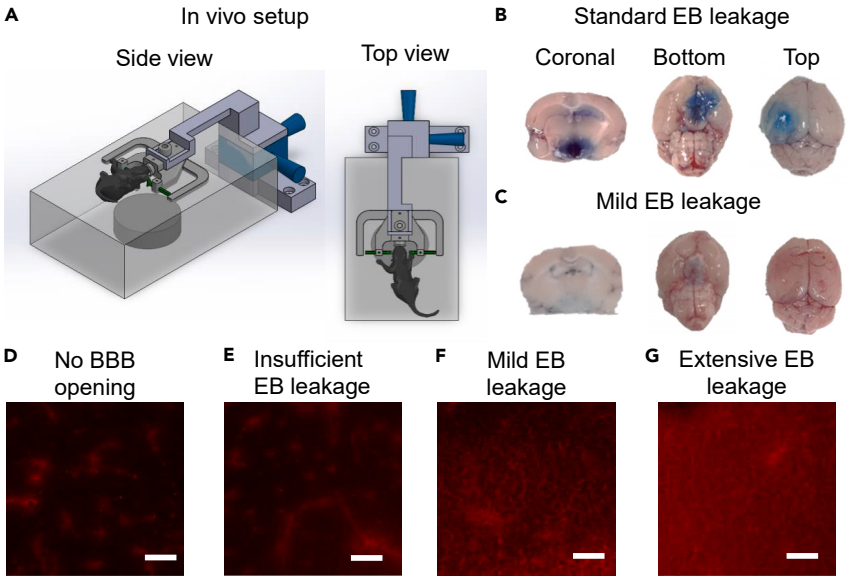

Figure 3. Evans blue extravasation following US-mediated BBBD

(A) *In vivo* setup. The mouse was mechanically positioned at the focal spot of an US transducer, located at the bottom of a water tank, using a custom holder.

(B) Standard EB leakage in treated brains, showing bright blue spots where BBBD was performed.

(C) Mild EB leakage in treated brains required for localizing BBBD at the resolution of a single blood vessel. Fluorescence microscopy images of EB leakage for: (D) No BBBD.

(E) Insufficient EB leakage.

(F) Mild EB leakage.

(G) Extensive EB leakage.

(D–G) 50 μm scale bars.

groups ($p > 0.05$, non-significant). This diameter distribution is consistent with previous reports of cerebral capillary diameters in mice.[38,43] The vasculature bifurcation density and length were also evaluated using the algorithm. Comparing these parameters for different brain areas revealed a significant increase in vascular density, in terms of length and bifurcation density in the cerebral cortex as compared to more ventral parts of the brain (hippocampus, hypothalamus, striatum, and thalamus) which is congruent with previous reports[27] (Figures 6C and 6D). No significant differences were found between the control and treated groups.

Next, the EB intensity in the perivascular area surrounding individual blood vessels was extracted and compared across diameter groups for different perivascular area parameters (Figure 7A). A comparison of the EB intensity histograms in a perivascular area of 10 pixels (2.9 μm width), for 3–4 and 9–10 μm blood vessels (Figures 7B and 7C), showed increased levels of EB intensity in the MB + FUS treated brains compared to the control brains ($p < 0.01$). In the control brains, a similar average EB intensity was observed for the two vessel diameters, whereas in the treated brains, EB intensity increased significantly for 9–10 μm blood vessels, compared to 3–4 μm ($p < 0.05$). Increased EB intensity as a function of vessel diameter, which is exclusive to MB + FUS treated vessels, was maintained when comparing different diameter groups in the range of 2–10 μm, and was not observed in the control groups (Figures S2 and 7D). In the treated brains, the EB intensity remained similar from 2 to 6 μm, but then started to increase monotonically with vasculature diameter. Changing the perivascular area parameters, such as the initial distance from the blood vessels used for the calculations, or the total distance from the blood vessel, did not significantly affect the results (Figure S3). For each blood vessel diameter histogram as shown in Figures 7B and 7C, the fraction of strong BBB opened blood vessels was calculated by setting a threshold based on a value of two standard deviations above the control mean for each diameter (95% confidence interval, dashed black line). The fraction of blood vessels in the MB + FUS treated group that exceeded this threshold was considered BBB opened. The percentage of strong BBBD also increased as a function of vessel diameter, from 9.75% for 2–3 μm blood vessels to 91.67% for 9–10 μm (Figure 7E). Overall, it can be seen that the EB intensity in the

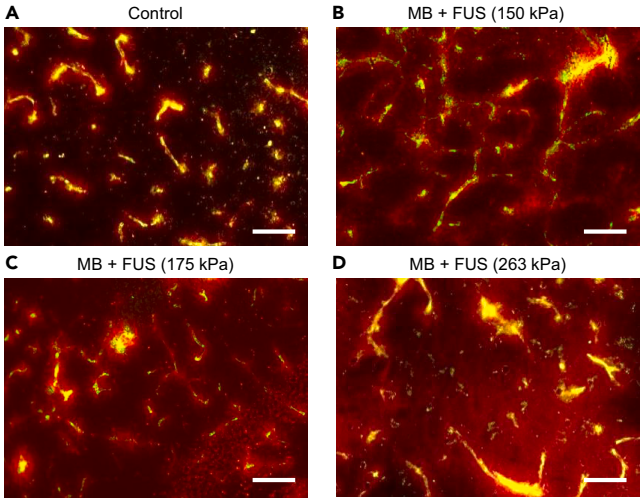

Figure 4. Microscopy images of brain slices

Blood vessels appear in green, whereas extravasated EB is red.

(A) Control brain without BBBD, where the green and red channels overlap.

(B–D) MB + FUS treated brain demonstrating increasing levels of EB extravasation to the perivascular area as a function of applied PNP: (B) 150 kPa, (C) 175 kPa, and (D) 263 kPa. Scale bars are 50 μm.

perivascular area of treated vessels (Figure 7D, blue bars), and the percentage of vessels undergoing strong BBBD (Figure 7E) presented a similar trend.

The effect of vasculature diameter dependent EB extravasation was evaluated as a function of applied PNP, for three insonation PNPs of 150, 175 and 263 kPa. 150 kPa was chosen as a low bound where mild BBB opening was observed, and 263 kPa represents the highest PNP where strong BBB opening with no microhemorrhage was detected. For the lower PNPs of 150 and 175 kPa, up to a diameter of 5–6 μm, no significant differences were observed compared to the control group (full statistical analysis is shown in Figure S4). In comparison, at these small diameters, the EB intensity around vessels treated with 263 kPa was significantly higher than in all other groups (control ($p < 0.0001$), 150 kPa ($p < 0.01$) and 175 kPa ($p < 0.01$)). EB intensity for diameters larger than 5–6 μm was significantly higher in all the treated brains, compared to the control group (Figure 8A). When calculating the fraction of strong BBBD vessels, all treated groups present a similar trend of increase as function of vessel diameter (Figure 8B). Our results indicate that 150 kPa is the threshold pressure for BBBD for blood vessels larger than 6 μm, and that BBBD of smaller vessels require higher PNP. Thus, BBBD depends both on blood vessel diameter and applied PNP.

DISCUSSION

In this article, we present a method for quantitative evaluation of FUS-mediated BBBD at a single blood vessel resolution. The method involves the injection of two fluorescent dyes, at specific time points that are carefully designed for localized extravasation across the BBB. Microscopy imaging of brain slices and an automated image processing algorithm is then used to characterize brain capillaries based on diameter and morphology, and assess the variation in BBBD as a function of blood vessel diameter. The focus of our research was on a capillary diameter range of 1–10 μm that was not studied in such detail so far. This range is particularly important because the majority of the blood vessels in the mouse brains are smaller than 10 μm. Furthermore, abnormalities and dysfunction in small capillaries play an important role in various brain pathologies,[44] such as cerebral small vessel disease which is one of the leading causes of stroke and cognitive decline in elderly,[45] and Alzheimer's disease which is the most common type of elderly dementia.[46] Therefore, the ability to conduct BBBD in capillaries is important for efficient drug delivery to brain diseases. The high resolution obtained with our method enables to precisely explore drug delivery to the brain from these capillaries, at diameter scales that were not feasible before. By being able to assess these smaller diameters, we detected significant changes in BBB opening as a function of blood vessel diameter. To label the blood vessels, the injection of a large MW green FITC-Dextran was used. Although large molecules, such as liposomes and cells,[39,47] have been

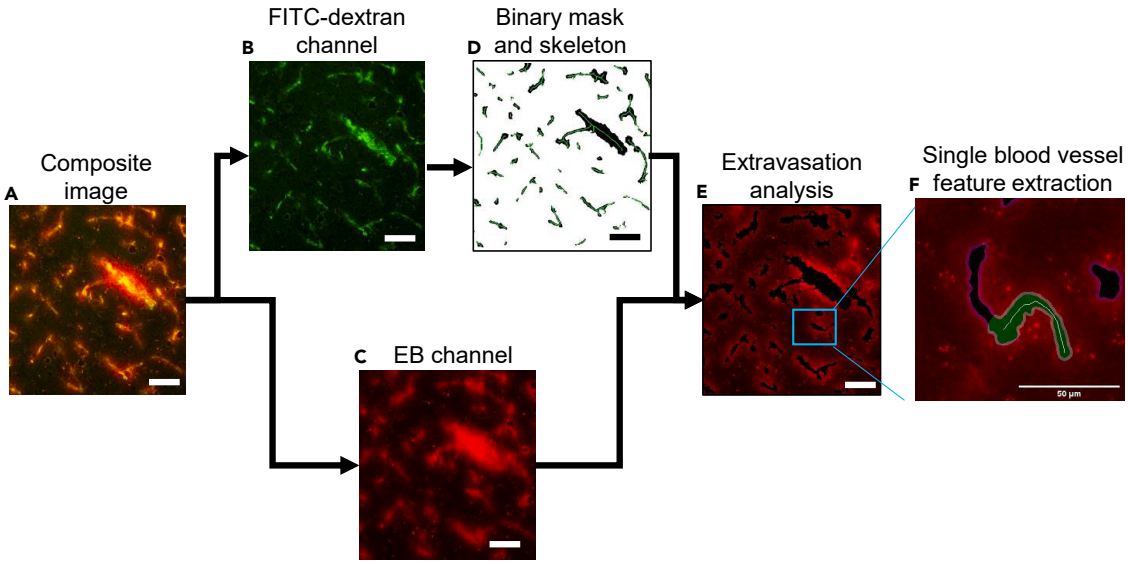

Figure 5. Image processing scheme

(A) The original composite image was split to two channels: (B) The green (FITC-Dextran) channel marking the blood vessels, and (C) the red, EB channel.
(D) Morphological operations were applied to (B) to perform vessel segmentation and skeleton extraction.
(E) The binary mask in (D) was applied to the EB channel in (C).
(F) The resulting image was used to determine the EB intensity in the perivascular ROI surrounding each vessel, and the vessel skeleton was used to extract the morphological features of each vessel. Finally, the median pixel intensity was quantified as a function of blood vessel diameter for the entire microvasculature population. Scale bars are 50 μm in all subfigures.

shown to cross the BBB following FUS-mediated BBBD, their diffusion times into the parenchyma are much longer. Here, mice were sacrificed 10 min post-injection, which suffices for efficient blood vessel staining by FITC-Dextran, without identified BBB penetration. Using fluorescence microscopy, the green FITC-Dextran channel was employed to segment the brain capillaries and extract their morphological features. The second dye was EB, which is a standard marker for blood vessel imaging[27] and is widely used for BBB opening identification and observation. Here, EB extravasation was probed for each individual blood vessel with and without FUS-mediated BBBD. The high spatial resolution and the ability to conduct single blood vessel extravasation quantification was challenging and required to carefully optimize the method's parameters. Therefore, all of the optimization steps were clearly described in the paper.

Applying the geometric blood vessel feature information, extracted from the green channel, to the red EB channel enabled us to quantify the diffusion of EB into the perivascular area surrounding each blood vessel. This method can quantify multiple parameters, such as the EB diffusion length, vascular density, vascular tortuosity, and microvasculature diameter. This is used to gauge EB intensity as a function of blood vessel diameter and compute the fraction of BBBD blood vessels. Our method is robust and can be used to gain important insights into unresolved questions related to FUS-mediated BBBD, such as the kinetics in capillaries with different diameters,[33,34] the impact of vasculature diameter on BBBD properties such as the duration of opening, the ability to deliver molecules of different sizes and their feasibility for brain drug delivery, and BBBD efficiency in different regions of the brain.[48] In addition, the method developed here can be used in future studies to assess the influence of multiple parameters that affect BBBD, such as MB gas volume that was shown previously to be significant in determining the extent of BBB opening,[17] and the influence of additional MB properties such as its shell composition and gas type. The ability to probe BBB opening at the microvasculature level could also aid in optimizing diffusion length for applications such as drug delivery to the proximal perivascular area while avoiding wide-spread perfusion throughout the parenchyma. Examples include brain tumor treatment for a perivascular space drug target,[49] or pericytes in various neurological disorders.[50] Another future application of the method involves evaluating the effects of local microvasculature density on BBB opening. Studies have shown that microvascular density differs considerably between different brain regions and patients,[51,52] which can lead to variations in BBB opening. Our platform is capable

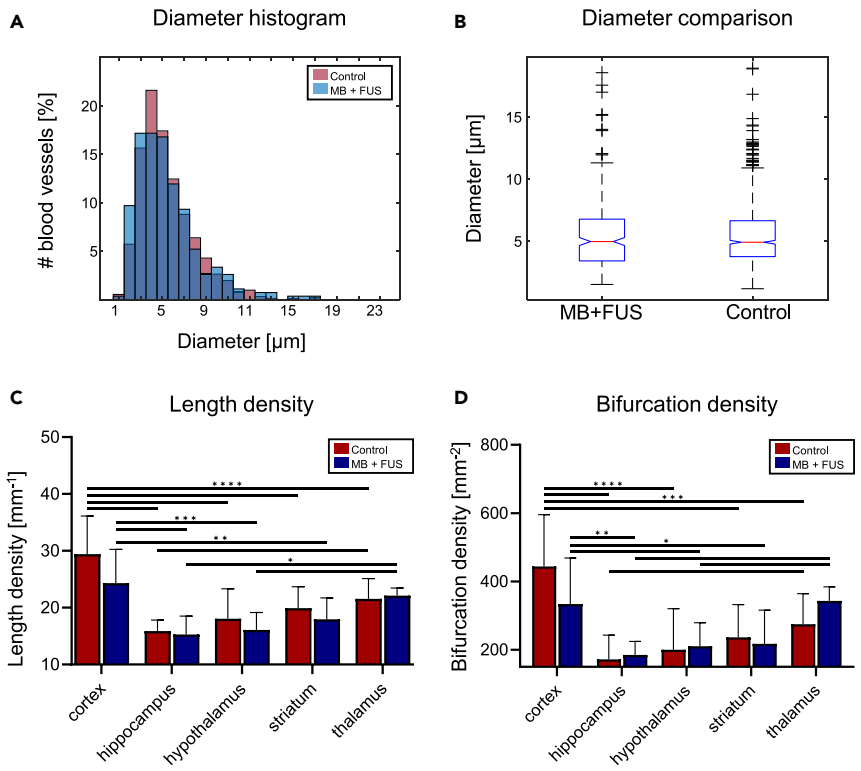

Figure 6. Blood vessel morphological characterization

(A) Microvasculature diameter histogram for the control and MB + FUS treated brains.

(B) Diameter comparison analysis for (A), Welch's t-test revealed no significant differences (total of n = 908 and n = 268 blood vessels for the control and MB + FUS groups, respectively). Vessel density analysis in different brain regions, (C) length density, (D) bifurcation density (total of n = 45 and n = 39 frames for the control and MB + FUS groups, respectively), Fisher's LSD test. The p values were *p < 0.05, **p < 0.01, ***p < 0.001, ****p < 0.0001. All data are plotted as the mean ± SD.

of assessing BBB openings at different regions while comparing the local vascular density, to identify variations.

Here, we focused on evaluating the effects of microvasculature diameter and PNP on the efficacy of BBBD. Variations in small blood vessels can be attributed to a combination of parameters. The first is reduced MB oscillations, that have been shown to be constrained in small tubes and blood vessels.[30,32,53] Another contributing parameter is the effective number of MBs. Although their concentration remains constant in the blood stream, given the smaller cross section of the capillaries, fewer MBs are present within these vessels compared to larger blood vessels. Similarly, smaller amounts of EB molecules flow within small capillaries, so that a gradual increase in EB intensity as a function of blood vessel diameter is expected; however, this was not the case for the results shown here. For a PNP of 263 kPa, EB extravasation remained almost constant for vessels smaller than 6 µm, and increased as function of diameter in larger vessels (Figure 7). At lower PNPs of 150 and 175 kPa, below 10% of blood vessels smaller than 6 µm were opened. Beyond 6 µm, the results exhibited a similar trend to 263 kPa, where the EB intensity in the perivascular area, and the fraction of BBB opened vessels were both increased significantly as a function of vessel diameter (Figures 8 and S4). Figure 8 demonstrates BBBD for all of the pressures that were tested. As such, because EB extravasation occurs via diffusion, once BBBD is achieved, we do not expect to see significant variations between pressures, unless BBBD threshold varies as a function of blood vessel diameter and insonation pressure, as observed here. For blood vessels larger than 6–7 µm BBBD is observed for all three PNP. For blood vessels smaller than 6 µm, there is a statistical significance between the 3 tested PNPs. Our results indicate that 150 kPa is the threshold pressure for BBBD for blood vessels larger than 6 µm. Smaller blood vessels show similar perivascular EB intensity

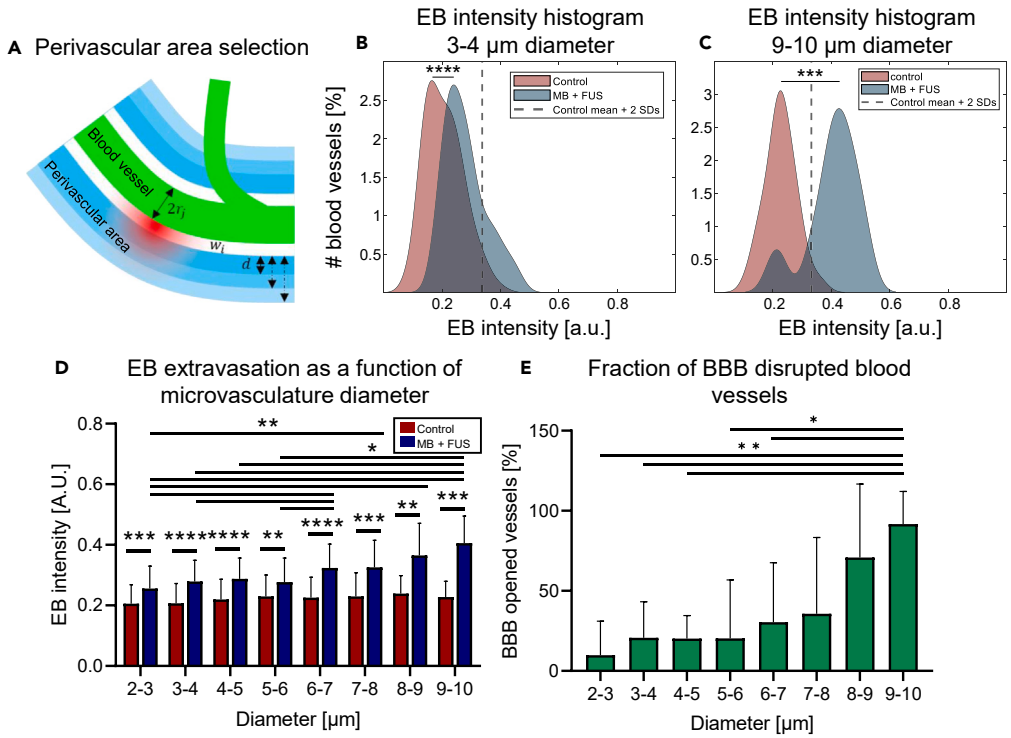

Figure 7. EB extravasation quantification as a function of blood vessel diameter

(A) The perivascular area around each blood vessel with a diameter of $2r_i$ was defined by its initial distance from the vessel wall (W_i) and total width (d). In each diameter group, the EB intensity in the perivascular area was calculated. The EB intensity histogram for blood vessels with diameters of (B) 3–4 µm, and (C) 9–10 µm. Welch's t-test.

(D) EB extravasation as a function of microvasculature diameter.

(E) Fraction of strong BBBD blood vessels.

(D and E) Mixed-effect model with Geisser-Greenhouse correction and the two-step step-up method for FDR control. The p values were *$p < 0.05$, **$p < 0.01$, ***$p < 0.001$, ****$p < 0.0001$. The data in (D,E) is plotted as mean ± SD.

as in the control group. For 263 kPa, BBBD was observed in all blood vessels' diameters, however stronger EB extravasation was detected around the larger vessels.

Compared to other methods that use 2PFM in mice,[33–36] our method can be applied to all brain regions, whereas *in vivo* 2PFM is limited mainly to superficial regions such as the cerebral cortex. Furthermore, our method utilizes a fast, simple approach that does not involve complex *in vivo* procedures such as craniotomies, or unique experimental setups. It also enables the imaging and processing of large brain regions, which facilitates the characterization of larger quantities of blood vessels simultaneously. Finally, the short scan duration used here compared to 2PFM enables the imaging of entire brain sections whilst maintaining the high spatial resolution required for imaging the capillary network, at a 1 µm vessel resolution.

PCD experiments were used to evaluate the MB vibrational response within different diameter blood vessel mimicking tubes. Although the two dimeters tested (280 and 100 µm) are both significantly larger than MBs, changes in MB echoes were detected, even when normalizing the results for volume within the fibers (Figure 1). Our findings suggest that stable cavitation initiates at lower sonication PNP within larger diameter fibers. We acknowledge that *in vivo*, the capillaries are smaller than the tubes used for the PCD experiments. To match the number of MBs between the different tube diameters, we placed a bundle of 100 µm tubes, such that the MB volume in both insonified regions will be similar. Reducing tube diameter further would necessitate a large number of parallel tubes, as the tube area increases exponentially with diameter, which poses severe technical limitations. Therefore, the PCD experiments were used as a perquisite step to identify variations as a function of tube diameter, followed by *in vivo* experiments to assess variations in capillaries. *in vivo*, because the sonication region is likely to include diverse diameters of blood vessels, lower PNP can be used to induce safe BBBD in larger vessel. However, at this lower PNP, reduced

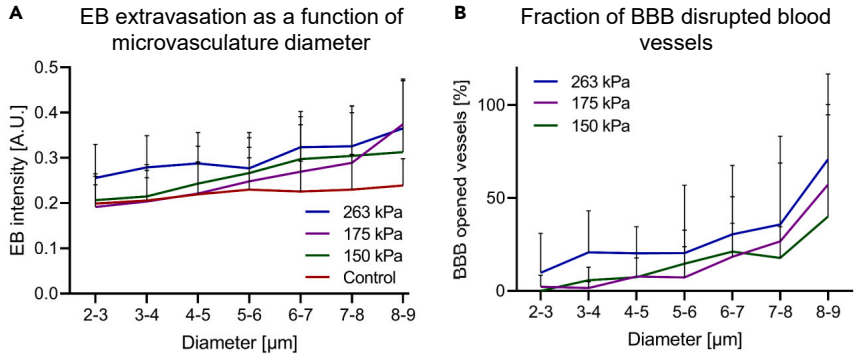

Figure 8. EB intensity quantification as a function of applied PNP and microvasculature diameter

(A) EB extravasation as a function of microvasculature diameter and applied PNP.

(B) Fraction of strong BBBD blood vessels as a function of applied PNP. All data are plotted as mean ± SD. Statistical analysis is shown in Figure S4.

stable cavitation in smaller capillaries may occur, causing less BBBD in these capillaries. The ICD also increased as a function of PNP in the two fiber diameters; however, the graph's slope has a steeper incline for the smaller fibers (Figure 1). This further narrows the PNP's operational range for safe BBB opening in smaller blood vessels.

MB responses depend crucially on the excitation frequency. A center frequency of 250 kHz was used here because this is a common frequency for noninvasive brain treatment. The low frequency facilitates skull penetration because of reduced attenuation.[3] However, at this low frequency range, MB oscillations are significantly enhanced so that there is only a narrow PNP range for safe BBBD.[24] The mechanism for these enhanced oscillations stems from the Blake threshold effect, which manifests as an infinite predicted bubble expansion beyond a critical PNP when the MBs are excited well below their resonance frequency. The PCD experiments confirm a sharp incline in MB vibrational response in both fiber diameters as a function of PNP, with a steeper slope in the smaller fibers. The current Blake threshold theory assumes that the bubbles are in free space. To fully predict MB behavior in different sized blood vessels, a modified Blake threshold effect that takes the effect of the surrounding blood vessels into account should be developed.

In vivo, the successful implementation of the single blood vessel BBBD assessment method developed here requires the following carefully controlled protocol components: Selection of US parameters (frequency, PNP and duration), titration and injection of the MBs and the two fluorescent dyes, as well as circulation times, brain harvesting, preservation, and slicing, microscopy imaging parameters, and the image processing algorithm. We showed that EB intensity increases with the microvasculature diameter, and that the fraction of vessels that undergo strong BBB openings also increases with diameter. EB was chosen here because it is a widely used molecule for BBBD visualization. However, EB is also known to diffuse quickly within the tissue. Thus, after a certain time following BBBD, the entire treated region will appear blue, and differences between blood vessels can no longer be distinguished.[36] Because EB eventually distributes across the tissue, it remains unclear whether the BBBD variations observed here at shorter time points have clinical significance. The image processing method here was used to characterize vascular features such as vessel length and bifurcation densities in different brain areas. Variations were observed between regions, with the highest length and bifurcation density in the cortex, which is consistent with previous reports.[27]

Limitations of the study

There are a number of study limitations that should be mentioned. First is that our transducer's focal spot was large, such that most of the brain regions were insonated. Nevertheless, BBBD was observed primarily in the hypothalamus region that was also characterized here to have a low vascular density (Figures 5C and 5D). This suggests that vascular density may also play a significant role in BBBD, and that lower density regions may be more susceptible to BBBD (e.g., higher PNPs are required for BBBD in other regions). In the current configuration, increasing the PNP will result in damage in the form of microhemorrhage in the hypothalamus region. A smaller focal spot generated by a larger transducer aperture or a higher frequency

could be used to induce BBBD more precisely, and the specific treatment parameters for each brain region can be optimized using our method.

In addition, this study focused on EB extravasation assessment. Although it is the most commonly used BBBD marker, it is a small molecule dye (~1 kDa) without a therapeutic value. This small molecular weight represents small anticancer drugs such as chemotherapy (<1 kDa).[54,55] It should be noted that there are various small molecules commonly used for the assessment of BBB opening such as Dextran-tetramethylrhodamine, Alexa-fluor-cadaverine, and Texas-Red-Dextran, with spectral properties that differ from FITC.[33,56] Therefore, the same study could be repeated to examine the penetration of these molecules. In future studies, larger molecules extravasation as a function of vasculature diameter will be assessed. Because the pharmacokinetics of each molecule is different, delivery of larger molecules will likely require calibrating the circulation duration.[57] From the therapeutic standpoint, 20 kDa molecules, match siRNA and miRNA (~14 kDa),[58–61] whereas 70 kDa corresponds to the size of proteins, macromolecules, and genes.[62–65] The method developed here can be used to optimize the delivery of a specific molecule using a fluorescent molecule with similar molecular weight and structural properties. For therapeutic applications, it is possible to link the drug of interest to a fluorescent marker and perform the method with the actual molecule. Alternatively, the therapeutic drug could be injected instead of the EB following BBBD. 10 min before brain harvesting, the large molecular weight FITC should be injected, to mark the blood vessels. Microscopy could then be used to analyze the therapeutic efficacy of the drug, as a function of the blood vessel diameter.

In terms of the microscopy imaging limitations, because the images taken here are two dimensional, whereas the blood vessels are three-dimensional, classification and accuracy could be affected. In the future, a tissue clearing method alongside 3D microscopy techniques such as light sheet microscopy, could be implemented with our method to assess BBBD volumetric effects as a function of microvasculature. Finally, in this study we did not quantify the amount of MBs within each vessel. Therefore, it is unclear whether the changes in MB cavitation are a function of the vessel diameter, the number of MBs within the vessel or the density of MBs within the vessel.

Overall, the robust method developed here showed that BBBD depends on capillary diameter. These variations can affect the pharmacokinetics of substances that are delivered across the BBB as a function of the local microvascular content. Therefore, the impact of blood vessel diameter should be considered when developing safe and reliable protocols for FUS-mediated BBBD. It is possible that the FUS-mediated BBBD should be optimized for specific regions, vascular diameters, and vascular densities. These parameters can vary as a function of target region, animal models, and may even diverge temporarily in the same region during vasodilative or vasoconstrictive events.[66] The method here can help identify these variations and should thus be included in the arsenal of BBBD characterization protocols. Moreover, it can be used to study BBB intactness integrity as a metric to evaluate and characterize conditions and diseases that affect the BBB, such as neurodegenerative conditions, cancer and inflammation.

STAR★METHODS

Detailed methods are provided in the online version of this paper and include the following:

- KEY RESOURCES TABLE
- RESOURCE AVAILABILITY
  - Lead contact
  - Materials availability
  - Data and code availability
- EXPERIMENTAL MODEL
- METHOD DETAILS
  - Microbubble preparation
  - Passive cavitation detection in blood vessel mimicking tubes
  - PCD data analysis
  - In-vivo BBBD
  - Microscopy imaging
  - Image processing
  - Hematoxylin & Eosin staining

SUPPLEMENTAL INFORMATION

Supplemental information can be found online at https://doi.org/10.1016/j.isci.2023.106965.

ACKNOWLEDGMENTS

This work was supported by funding from Insightec Ltd., the Israel Science Foundation (grant numbers 192/22 and 3450/20), the Israel Ministry of Science & Technology (grant number 101716), an ERC StG grant no. 101041118 (NanoBubbleBrain), a Zimin Institute grant, and was partially supported by a grant from the Nicholas and Elizabeth Slezak Super Center for Cardiac Research and Biomedical Engineering at Tel Aviv University.

AUTHOR CONTRIBUTIONS

S.K. designed and performed all the research and wrote the paper. R.G., L.P., R.Z., and Y.H. assisted with the *in vivo* experiments, microscopy, and image processing. T.I. advised and designed the research and wrote the paper. All authors have approved the final version of this manuscript.

DECLARATION OF INTERESTS

The authors have declared that no competing interest exists.

Received: February 14, 2023
Revised: May 1, 2023
Accepted: May 22, 2023
Published: May 26, 2023

REFERENCES

1. Meng, Y., Hynynen, K., and Lipsman, N. (2021). Applications of focused ultrasound in the brain: from thermoablation to drug delivery. Nat. Rev. Neurol. *17*, 7–22. https://doi.org/10.1038/s41582-020-00418-z.

2. Pardridge, W.M. (2005). The blood-brain barrier: bottleneck in brain drug development. NeuroRx *2*, 3–14. https://doi.org/10.1007/bf03206638.

3. Hynynen, K., and Jolesz, F.A. (1998). Demonstration of potential noninvasive ultrasound brain therapy through an intact skull. Ultrasound Med. Biol. *24*, 275–283. https://doi.org/10.1016/S0301-5629(97)00269-X.

4. Krishna, V., Sammartino, F., and Rezai, A. (2018). A review of the current therapies, challenges, and future directions of transcranial focused ultrasound Technology advances in diagnosis and treatment. JAMA Neurol. *75*, 246–254. https://doi.org/10.1001/jamaneurol.2017.3129.

5. Lipsman, N., Meng, Y., Bethune, A.J., Huang, Y., Lam, B., Masellis, M., Herrmann, N., Heyn, C., Aubert, I., Boutet, A., et al. (2018). Blood–brain barrier opening in Alzheimer's disease using MR-guided focused ultrasound. Nat. Commun. *9*, 2336. https://doi.org/10.1038/s41467-018-04529-6.

6. Tung, Y.S., Vlachos, F., Feshitan, J.A., Borden, M.A., and Konofagou, E.E. (2011). The mechanism of interaction between focused ultrasound and microbubbles in blood-brain barrier opening in mice. J. Acoust. Soc. Am. *130*, 3059–3067. https://doi.org/10.1121/1.3646905.

7. Chen, K.-T., Lin, Y.-J., Chai, W.-Y., Lin, C.-J., Chen, P.-Y., Huang, C.-Y., Kuo, J.S., Liu, H.-L., and Wei, K.-C. (2020). Neuronavigation-guided focused ultrasound (NaviFUS) for transcranial blood-brain barrier opening in recurrent glioblastoma patients: clinical trial protocol. Ann. Transl. Med. *8*, 673. https://doi.org/10.21037/atm-20-344.

8. Mainprize, T., Lipsman, N., Huang, Y., Meng, Y., Bethune, A., Ironside, S., Heyn, C., Alkins, R., Trudeau, M., Sahgal, A., et al. (2019). Blood-brain barrier opening in primary brain tumors with non-invasive MR-guided focused ultrasound: a clinical safety and feasibility study. Sci. Rep. *9*, 321. https://doi.org/10.1038/s41598-018-36340-0.

9. Tung, Y.-S., Choi, J.J., Baseri, B., and Konofagou, E.E. (2010). Identifying the inertial cavitation threshold and skull effects in a vessel phantom using focused ultrasound and microbubbles. Ultrasound Med. Biol. *36*, 840–852. https://doi.org/10.1016/j.ultrasmedbio.2010.02.009.

10. Xu, S., Ye, D., Wan, L., Shentu, Y., Yue, Y., Wan, M., and Chen, H. (2019). Correlation between brain tissue damage and inertial cavitation dose quantified using passive cavitation imaging. Ultrasound Med. Biol. *45*, 2758–2766. https://doi.org/10.1016/j.ultrasmedbio.2019.07.004.

11. Stride, E., and Saffari, N. (2004). Theoretical and experimental investigation of the behaviour of ultrasound contrast agent particles in whole blood. Ultrasound Med. Biol. *30*, 1495–1509. https://doi.org/10.1016/j.ultrasmedbio.2004.09.003.

12. Wu, S.Y., Tung, Y.S., Marquet, F., Downs, M., Sanchez, C., Chen, C., Ferrera, V., and Konofagou, E. (2014). Transcranial cavitation detection in primates during blood-brain barrier opening-a performance assessment study. IEEE Trans. Ultrason. Ferroelectr. Freq. Control *61*, 966–978. https://doi.org/10.1109/TUFFC.2014.2992.

13. Kamimura, H.A., Flament, J., Valette, J., Cafarelli, A., Badin, R.A., Hantraye, P., and Larrat, B.B. Feedback control of microbubble cavitation for ultrasound-mediated blood-brain barrier disruption in non-human primates under magnetic resonance guidance. J. Cereb. Blood Flow Metab. 39, 1191–1203. https://doi.org/10.1177/0271678X17753514.

14. Tung, Y.-S., Vlachos, F., Choi, J.J., Deffieux, T., Selert, K., and Konofagou, E.E. (2010). In vivo transcranial cavitation threshold detection during ultrasound-induced blood–brain barrier opening in mice. Phys. Med.

Biol. *55*, 6141–6155. https://doi.org/10.1088/0031-9155/55/20/007.

15. Bing, C., Hong, Y., Hernandez, C., Rich, M., Cheng, B., Munaweera, I., Szczepanski, D., Xi, Y., Bolding, M., Exner, A., et al. (2018). Characterization of different bubble formulations for blood-brain barrier opening using a focused ultrasound system with acoustic feedback control. Sci. Rep. *8*, 7986. https://doi.org/10.1038/s41598-018-26330-7.

16. Samiotaki, G., Vlachos, F., Tung, Y.-S., and Konofagou, E.E. (2012). A quantitative pressure and microbubble-size dependence study of focused ultrasound-induced blood-brain barrier opening reversibility in vivo using MRI. Magn. Reson. Med. *67*, 769–777. https://doi.org/10.1002/mrm.23063.

17. Song, K.H., Fan, A.C., Hinkle, J.J., Newman, J., Borden, M.A., and Harvey, B.K. (2017). Microbubble gas volume: a unifying dose parameter in blood-brain barrier opening by focused ultrasound. Theranostics *7*, 144–152. https://doi.org/10.7150/thno.15987.

18. Ilovitsh, T., Feng, Y., Foiret, J., Kheirolomoom, A., Zhang, H., Ingham, E.S., Ilovitsh, A., Tumbale, S.K., Fite, B.Z., Wu, B., et al. (2020). Low-frequency ultrasound-mediated cytokine transfection enhances T cell recruitment at local and distant tumor sites. Proc. Natl. Acad. Sci. USA *117*, 12674–12685. https://doi.org/10.1073/pnas.1914906117.

19. Bismuth, M., Katz, S., Rosenblatt, H., Twito, M., Aronovich, R., and Ilovitsh, T. (2022). Acoustically detonated microbubbles coupled with low frequency insonation: multiparameter evaluation of low energy mechanical ablation. Bioconjug. Chem. *33*, 1069–1079. https://doi.org/10.1021/acs.bioconjchem.1c00203.

20. Bismuth, M., Katz, S., Mano, T., Aronovich, R., Hershkovitz, D., Exner, A.A., and Ilovitsh, T. (2022). Low frequency nanobubble-enhanced ultrasound mechanotherapy for noninvasive cancer surgery. Nanoscale *14*, 13614–13627. https://doi.org/10.1039/d2nr01367c.

21. Glickstein, B., Levron, M., Shitrit, S., Aronovich, R., Feng, Y., and Ilovitsh, T. (2022). Nanodroplet-mediated low-energy mechanical ultrasound surgery. Ultrasound Med. Biol. *48*, 1229–1239. https://doi.org/10.1016/j.ultrasmedbio.2022.02.018.

22. Glickstein, B., Aronovich, R., Feng, Y., and Ilovitsh, T. (2022). Development of an ultrasound guided focused ultrasound system for 3D volumetric low energy nanodroplet-mediated histotripsy. Sci. Rep. *12*, 20664. https://doi.org/10.1038/s41598-022-25129-x.

23. Eck, M., Aronovich, R., and Ilovitsh, T. (2022). Efficacy optimization of low frequency microbubble-mediated sonoporation as a drug delivery platform to cancer cells. Int. J. Pharm. X *4*, 100132. https://doi.org/10.1016/j.ijpx.2022.100132.

24. Ilovitsh, T., Ilovitsh, A., Foiret, J., Caskey, C.F., Kusunose, J., Fite, B.Z., Zhang, H., Mahakian, L.M., Tam, S., Butts-Pauly, K., et al. (2018). Enhanced microbubble contrast agent oscillation following 250 kHz insonation. Sci. Rep. *8*, 16347. https://doi.org/10.1038/s41598-018-34494-5.

25. Smith, A.F., Doyeux, V., Berg, M., Peyrounette, M., Haft-Javaherian, M., Larue, A.E., Slater, J.H., Lauwers, F., Blinder, P., Tsai, P., et al. (2019). Brain capillary networks across species: a few simple organizational requirements are sufficient to reproduce both structure and function. Front. Physiol. *10*, 233. https://doi.org/10.3389/fphys.2019.00233.

26. Wong, A.D., Ye, M., Levy, A.F., Rothstein, J.D., Bergles, D.E., Searson, P.C., Nadeau, J., and Sharma, H.S. (2013). The blood-brain barrier: an engineering perspective. Front. Neuroeng. *6*, 7. https://doi.org/10.3389/fneng.2013.00007.

27. Todorov, M.I., Paetzold, J.C., Schoppe, O., Tetteh, G., Shit, S., Efremov, V., Todorov-Völgyi, K., Düring, M., Dichgans, M., Piraud, M., et al. (2020). Machine learning analysis of whole mouse brain vasculature. Nat. Methods *17*, 442–449. https://doi.org/10.1038/s41592-020-0792-1.

28. Cipolla, M.J. (2009). Control of cerebral blood flow. In The Cerebral Circulation (Morgan & Claypool Life Sciences).

29. Caskey, C.F., Stieger, S.M., Qin, S., Dayton, P.A., and Ferrara, K.W. (2007). Direct observations of ultrasound microbubble contrast agent interaction with the microvessel wall. J. Acoust. Soc. Am. *122*, 1191–1200. https://doi.org/10.1121/1.2747204.

30. Caskey, C.F., Kruse, D.E., Dayton, P.A., Kitano, T.K., and Ferrara, K.W. (2006). Microbubble oscillation in tubes with diameters of 12, 25, and 195 microns. Appl. Phys. Lett. *88*, 033902. https://doi.org/10.1063/1.2164392.

31. Hingot, V., Errico, C., Heiles, B., Rahal, L., Tanter, M., and Couture, O. (2019). Microvascular flow dictates the compromise between spatial resolution and acquisition time in Ultrasound Localization Microscopy. Sci. Rep. *9*, 2456. https://doi.org/10.1038/s41598-018-38349-x.

32. Zheng, H., Dayton, P.A., Caskey, C., Zhao, S., Qin, S., and Ferrara, K.W. (2007). Ultrasound-driven microbubble oscillation and translation within small phantom vessels. Ultrasound Med. Biol. *33*, 1978–1987. https://doi.org/10.1016/j.ultrasmedbio.2007.06.007.

33. Cho, E.E., Drazic, J., Ganguly, M., Stefanovic, B., and Hynynen, K. (2011). Two-photon fluorescence microscopy study of cerebrovascular dynamics in ultrasound-induced blood–brain barrier opening. J. Cereb. Blood Flow Metab. *31*, 1852–1862. https://doi.org/10.1038/JCBFM.2011.59.

34. Nhan, T., Burgess, A., Cho, E.E., Stefanovic, B., Lilge, L., and Hynynen, K. (2013). Drug delivery to the brain by focused ultrasound induced blood-brain barrier disruption: quantitative evaluation of enhanced permeability of cerebral vasculature using two-photon microscopy. J. Control. Release *172*, 274–280. https://doi.org/10.1016/j.jconrel.2013.08.029.

35. Poon, C., Pellow, C., and Hynynen, K. (2021). Neutrophil recruitment and leukocyte response following focused ultrasound and microbubble mediated blood-brain barrier treatments. Theranostics *11*, 1655–1671. https://doi.org/10.7150/thno.52710.

36. Xia, L., Hu, L., Hu, M., Chen, X., Chen, S., and Shen, Y. (2021). Observation of the Blood-Brain Barrier Opening by Ultrasound with Microbubbles on Mice Using Intravital Imaging with Two-Photon Microscopy (IEEE International Ultrasonics Symposium, IUS), pp. 2–5. https://doi.org/10.1109/IUS52206.2021.9593513.

37. Stefanovic, B., Hutchinson, E., Yakovleva, V., Schram, V., Russell, J.T., Belluscio, L., Koretsky, A.P., and Silva, A.C. (2008). Functional reactivity of cerebral capillaries. J. Cereb. Blood Flow Metab. *28*, 961–972. https://doi.org/10.1038/SJ.JCBFM.9600590.

38. Bennett, R.E., Robbins, A.B., Hu, M., Cao, X., Betensky, R.A., Clark, T., Das, S., and Hyman, B.T. (2018). Tau induces blood vessel abnormalities and angiogenesis-related gene expression in P301L transgenic mice and human Alzheimer's disease. Proc. Natl. Acad. Sci. USA *115*, E1289–E1298. https://doi.org/10.1073/pnas.1710329115.

39. Burgess, A., Ayala-Grosso, C.A., Ganguly, M., Jordão, J.F., Aubert, I., and Hynynen, K. (2011). Targeted delivery of neural stem cells to the brain using MRI-guided focused ultrasound to disrupt the blood-brain barrier. PLoS One *6*, e27877. https://doi.org/10.1371/journal.pone.0027877.

40. Nagaraja, T.N., Keenan, K.A., Fenstermacher, J.D., and Knight, R.A. (2008). Acute leakage patterns of fluorescent plasma flow markers after transient focal cerebral ischemia suggest large openings in blood-brain barrier. Microcirculation *15*, 1–14. https://doi.org/10.1080/10739680701409811.

41. Wolman, M., Klatzo, I., Chui, E., Wilmes, F., Nishimoto, K., Fujiwara, K., and Spatz, M. (1981). Evaluation of the dye-protein tracers in pathophysiology of the blood-brain barrier. Acta Neropathol. *54*, 55–61.

42. Xu, Y., He, Q., Wang, M., Wang, X., Gong, F., Bai, L., Zhang, J., and Wang, W. (2019). Quantifying blood-brain-barrier leakage using a combination of evans blue and high molecular weight FITC-Dextran. J. Neurosci. Methods *325*, 108349. https://doi.org/10.1016/j.jneumeth.2019.108349.

43. Hall, C.N., Reynell, C., Gesslein, B., Hamilton, N.B., Mishra, A., Sutherland, B.A., Oâ Farrell, F.M., Buchan, A.M., Lauritzen, M., and Attwell, D. (2014). Capillary pericytes regulate cerebral blood flow in health and disease. Nature *508*, 55–60. https://doi.org/10.1038/nature13165.

44. Erdener, Ş.E., and Dalkara, T. (2019). Small vessels are a big problem in neurodegeneration and neuroprotection. Front. Neurol. *10*, 889. https://doi.org/10.3389/fneur.2019.00889.

45. Østergaard, L., Engedal, T.S., Moreton, F., Hansen, M.B., Wardlaw, J.M., Dalkara, T., Markus, H.S., and Muir, K.W. (2016). Cerebral

small vessel disease: capillary pathways to stroke and cognitive decline. J. Cereb. Blood Flow Metab. *36*, 302–325. https://doi.org/10.1177/0271678X15606723.

46. Cruz Hernández, J.C., Bracko, O., Kersbergen, C.J., Muse, V., Haft-Javaherian, M., Berg, M., Park, L., Vinarcsik, L.K., Ivasyk, I., Rivera, D.A., et al. (2019). Neutrophil adhesion in brain capillaries reduces cortical blood flow and impairs memory function in Alzheimer's disease mouse models. Nat. Neurosci. *22*, 413–420. https://doi.org/10.1038/s41593-018-0329-4.

47. Lin, C.Y., Hsieh, H.Y., Pitt, W.G., Huang, C.Y., Tseng, I.C., Yeh, C.K., Wei, K.C., and Liu, H.L. (2015). Focused ultrasound-induced blood-brain barrier opening for non-viral, non-invasive, and targeted gene delivery. J. Control. Release *212*, 1–9. https://doi.org/10.1016/J.JCONREL.2015.06.010.

48. Lapin, N.A., Gill, K., Shah, B.R., and Chopra, R. (2020). Consistent opening of the blood brain barrier using focused ultrasound with constant intravenous infusion of microbubble agent. Sci. Rep. *10*, 16546. https://doi.org/10.1038/s41598-020-73312-9.

49. Seano, G. (2018). Targeting the perivascular niche in brain tumors. Curr. Opin. Oncol. *30*, 54–60. https://doi.org/10.1097/CCO.0000000000000417.

50. Cheng, J., Korte, N., Nortley, R., Sethi, H., Tang, Y., and Attwell, D. (2018). Targeting pericytes for therapeutic approaches to neurological disorders. Acta Neuropathol. *136*, 507–523. https://doi.org/10.1007/s00401-018-1893-0.

51. Kubíková, T., Kochová, P., Tomášek, P., Witter, K., and Tonar, Z. (2018). Numerical and length densities of microvessels in the human brain: correlation with preferential orientation of microvessels in the cerebral cortex, subcortical grey matter and white matter, pons and cerebellum. J. Chem. Neuroanat. *88*, 22–32. https://doi.org/10.1016/J.JCHEMNEU.2017.11.005.

52. Hase, Y., Ding, R., Harrison, G., Hawthorne, E., King, A., Gettings, S., Platten, C., Stevenson, W., Craggs, L.J.L., and Kalaria, R.N. (2019). White matter capillaries in vascular and neurodegenerative dementias. Acta Neuropathol. Commun. *7*, 16. https://doi.org/10.1186/s40478-019-0666-x.

53. Chen, H., Brayman, A.A., and Matula, T.J. (2010). The peculiar interactions of microbubbles and microvessels. In 20th International Congress on Acoustics20th International Congress on Acoustics.

54. Maciulevičius, M., Tamošiūnas, M., Navickaitė, D., Šatkauskas, S., and Venslauskas, M.S. (2022). Free- and liposomal- doxorubicin delivery via microbubble inertial cavitation. SSRN Electron. J. *72*, 103386. https://doi.org/10.2139/ssrn.3981539.

55. Jackson, J.K., Pirmoradi, F.N., Wan, C.P.L., Siu, T., Chiao, M., and Burt, H.M. (2011). Increased accumulation of paclitaxel and doxorubicin in proliferating capillary cells and prostate cancer cells following ultrasound exposure. Ultrasonics *51*, 932–939. https://doi.org/10.1016/j.ultras.2011.05.008.

56. Yanagida, K., Liu, C.H., Faraco, G., Galvani, S., Smith, H.K., Burg, N., Anrather, J., Sanchez, T., Iadecola, C., and Hla, T. (2017). Size-selective opening of the blood-brain barrier by targeting endothelial sphingosine 1-phosphate receptor 1. Proc. Natl. Acad. Sci. USA *114*, 4531–4536. https://doi.org/10.1073/pnas.1618659114.

57. Choi, J.J., Wang, S., Tung, Y.S., Morrison, B., and Konofagou, E.E. (2010). Molecules of various pharmacologically-relevant sizes can cross the ultrasound-induced blood-brain barrier opening in vivo. Ultrasound Med. Biol. *36*, 58–67. https://doi.org/10.1016/j.ultrasmedbio.2009.08.006.

58. Karki, A., Giddings, E., Carreras, A., Champagne, D., Fortner, K., Rincon, M., and Wu, J. (2019). Sonoporation as an Approach for siRNA delivery into T cells. Ultrasound Med. Biol. *45*, 3222–3231. https://doi.org/10.1016/j.ultrasmedbio.2019.06.406.

59. Ha, C.H., Lee, S.C., Kim, S., Chung, J., Bae, H., and Kwon, K. (2015). Novel mechanism of gene transfection by low-energy shock wave. Sci. Rep. *5*, 12843. https://doi.org/10.1038/srep12843.

60. Kinoshita, M., and Hynynen, K. (2005). A novel method for the intracellular delivery of siRNA using microbubble-enhanced focused ultrasound. Biochem. Biophys. Res. Commun. *335*, 393–399. https://doi.org/10.1016/j.bbrc.2005.07.101.

61. Mullick Chowdhury, S., Wang, T.Y., Bachawal, S., Devulapally, R., Choe, J.W., Abou Elkacem, L., Yakub, B.K., Wang, D.S., Tian, L., Paulmurugan, R., et al. (2016). Ultrasound-guided therapeutic modulation of hepatocellular carcinoma using complementary microRNAs. J. Control. Release *238*, 272–280. https://doi.org/10.1016/j.jconrel.2016.08.005.

62. Liu, X., Wu, F., Ji, Y., and Yin, L. (2019). Recent advances in anti-cancer protein/peptide delivery. Bioconjug. Chem. *30*, 305–324. https://doi.org/10.1021/acs.bioconjchem.8b00750.

63. Dreher, M.R., Liu, W., Michelich, C.R., Dewhirst, M.W., Yuan, F., and Chilkoti, A. (2006). Tumor vascular permeability, accumulation, and penetration of macromolecular drug carriers. J. Natl. Cancer Inst. *98*, 335–344. https://doi.org/10.1093/jnci/djj070.

64. Matsunaga, W., Ichikawa, M., Nakamura, A., Ishikawa, T., and Gotoh, A. (2018). Lentiviral vector-mediated gene transfer in human bladder cancer cell lines. Anticancer Res. *38*, 2015–2020. https://doi.org/10.21873/anticanres.12440.

65. Wang, Y.U., Chen, Y.N., Zhang, W., Yang, Y.U., Bai, W.K., Shen, E., and Hu, B. (2016). Upregulation of ULK1 expression in PC-3 cells following tumor protein P53 transfection by sonoporation. Oncol. Lett. *11*, 699–704. https://doi.org/10.3892/ol.2015.3946.

66. Fan, J.L., Rivera, J.A., Sun, W., Peterson, J., Haeberle, H., Rubin, S., and Ji, N. (2020). High-speed volumetric two-photon fluorescence imaging of neurovascular dynamics. Nat. Commun. *11*, 6020. https://doi.org/10.1038/s41467-020-19851-1.

67. Farny, C.H., Holt, R.G., and Roy, R.A. (2009). Temporal and spatial detection of HIFU-induced inertial and hot-vapor cavitation with a diagnostic ultrasound system. Ultrasound Med. Biol. *35*, 603–615. https://doi.org/10.1016/j.ultrasmedbio.2008.09.025.

68. Corliss, B.A., Doty, R., Mathews, C., Yates, P.A., Zhang, T., and Peirce, S.M. (2019). REAVER: improved analysis of high-resolution vascular network images revealed through round-robin rankings of accuracy and precision. Preprint at bioRxiv. https://doi.org/10.1101/707570.

STAR★METHODS

KEY RESOURCES TABLE

REAGENT or RESOURCE	SOURCE	IDENTIFIER
Chemicals, peptides, and recombinant proteins		
Perfluorobutane (C_4F_{10})	F2 Chemicals LTD	CAS: 355-25-9
Distearoylphosphatidylcholine (DSPC)	Avanti Polar Lipids	850365C, CAS: 816-94-4
18:0 PEG2000 PE	Avanti Polar Lipids	880120, CAS: 474922-77-5
Glycerol	Sigma-Aldrich	G5516, CAS: 56-81-5
propylene glycol	Sigma-Aldrich	BP868, CAS: 57-55-6
Saline	Fischer scientific	Z1376, CAS: 7647-14-5
agarose powder	Holland Moran	400402500, CAS: 9002-18-0
Dulbecco's phosphate buffered saline	Biological Industries Israel	02-023-1A
isoflurane	USP	1349003, CAS: 26675-46-7
Evans Blue Dye	Sigma-Aldrich	E2129, CAS: 314-13-6
Fluorescein isothiocyanate–Dextran 2000	Sigma-Aldrich	52471, CAS: 60842-46-8
OCT cryo compound	Leica Biosystems	14020108926
Paraformaldehyde	Fisher Scientific	50-259-99
Hematoxylin Stain	Leica Biosystems	3801542
Eosin Secondary-Counter Stain	Leica Biosystems	3801602
Deposited data		
Example microscopy data	This paper	https://zenodo.org/badge/latestdoi/637521961
Experimental models: Organisms/strains		
Female C57BL/6 mice (10–11 weeks old, 16-21gr)	Envigo	C57BL/6JOlaHsd
Software and algorithms		
MATLAB	The MathWorks, Inc.	https://www.mathworks.com/products/matlab.html
Rapid Editable Analysis of Vessel Elements Routine (REAVER)	Corliss et al.[68]	https://github.com/uva-peirce-cottler-lab/public_REAVER
Image processing and data analysis software	This paper	https://zenodo.org/badge/latestdoi/637521961
Prism	GraphPad	https://www.graphpad.com/
Other		
AccuSizer® FX-Nano, Particle Sizing Systems	Entegris	A9AD 000
250 kHz, single element, focused ultrasound transducer	Sonic Concepts	H115
Arbitrary/Function generator	Tektronix Inc.	AFG1012
Laboratory Linear Power Amplifier	E&I	2100L
Transducer Power Output™	Sonic Concepts	TPO-200
Needle hydrophone	NH0500	Precision Acoustics
280 μm ID PTFE tube	Instech laboratories Inc.	BTPE-10
100 μm ID PTFE tube	Zeus	Sub-Lite-Wall®
Phased array ultrasound transducer	Philips	ATL P4-1
Vantage™ Research Ultrasound System	Verasonics Inc.	Vantage 256
Low-Flow Electronic Vaporizer	Kent Scientific	SomnoFlo
cryostat microtome	Leica Biosystems	CM1950
Automated Fluorescence Microscope	Olympus life science	BX63
×20 microscope objective	Olympus life science	UPLFLN 20X

RESOURCE AVAILABILITY

Lead contact

Further information and requests for resources and data should be directed to and will be fulfilled by the lead contact, Tali Ilovitsh (ilovitsh@tauex.tau.ac.il).

Materials availability

This study did not generate new unique reagents.

Data and code availability

All original code has been deposited at Zenodo and is publicly available as of the date of publication together with a set of example microscopy images. DOIs are listed in the key resources table. Additional data will be shared by the lead contact upon request. Any additional information required to analyze the data reported in this paper is available from the lead contact upon request.

EXPERIMENTAL MODEL

A total of 110 mice were used in the *in vivo* experiments. Female C57BL/6 mice (10–11 weeks old, 16-21g, Envigo, Jerusalem, Israel) were used. All the animal experiments were conducted in accordance with the Guide for the Care and Use of Laboratory Animals and approved by the Institutional Animal Care and Use Committee at Tel-Aviv University.

METHOD DETAILS

Microbubble preparation

MBs were prepared and measured as described in previous studies.[24] The MBs were composed of a phospholipid shell and a Perfluorobutane (C_4F_{10}) gas core. The lipids (2.5 mg per 1mL) were Distearoyl-phosphatidylcholine (DSPC; 850365C) and 1,2-distearoyl-*sn*-glycero-3-phosphoethanolamine-N-[methoxy (polyethylene glycol)-2000] (ammonium salt) (DSPE-PEG2000PE; 880120) which were combined at a molar ratio of 90:10 and made using a thin film hydration method. A buffer (mixture of glycerol (10%), propylene glycol (10%) and saline (80%) (pH 7.4)) was added to the lipids and sonicated at 62°C. The MB precursor solution was aliquoted into vials with liquid volume of 1 mL and saturated with perfluorobutane. Upon use, the vials were shaken for 45 s in a vial shaker and purified via centrifugation to remove MBs smaller than 0.5 μm in radii. Size selection was applied as described previously to remove MBs larger than 5 μm in diameter. The size and concentration of the MBs were measured twice with a particle counter system (AccuSizer FX-Nano, Particle Sizing Systems, Entegris, MA, USA). The bubbles were used within 3 h of their preparation. The size distribution and concentration varied by less than 10% between the measurements.

Passive cavitation detection in blood vessel mimicking tubes

The US setup (Illustrated in Figure 1A) was composed of a spherical single element FUS transducer (H115, Sonic Concepts, Bothell, WA, USA), operating at 250 kHz center frequency, with a focal distance of 45 mm, and an aperture diameter of 64 mm. The transducer was located at the bottom of a water tank, facing upwards. This transducer was operated either by a function generator (AFG1012, Tektronix Inc., Beaverton, OR USA) and an RF amplifier (2100L, Electronics & Innovation, Ltd., Rochester, NY, USA) for the fiber experiments, or a transducer power output system (TPO-200, Sonic Concepts, Bothell, WA, USA) for the *in vivo* experiments. The PNP at the focal spot was calibrated using a needle hydrophone (NH0500, Precision Acoustics, UK). Pure agarose phantom embedding blood vessel mimicking tubes were placed at the transducer focal spot. These agarose phantoms were prepared by mixing 1.5% agarose powder (A10752, Alfa Caesar, MA, USA) and deionized water. The solution was heated until all the powder had completely dissolved, and then was poured into a custom laser-cut mold. The mold measured 65 mm × 29 mm × 25 mm (length x width x height) and contained a hole in the parallel sides to insert the tubes. The PTFE tubes had inner diameters of either 280 μm (BTPE-10, Instech laboratories Inc., Plymouth meeting, PA, USA), or 100 μm (PTFE Extruded Sub-Lite-Wall Zeus, Orangeburg, SC, USA). Because the liquid volume, and hence the quantity of MBs was larger within the 280 μm tubes, three 100 μm tubes were connected in parallel to increase the total cross-section. An imaging phased array transducer (ATL P4-1, Philips, Seattle, WA, USA) was placed perpendicularly to the agarose phantom, and to the FUS transducer, and was aligned to focus on the tube. This transducer was controlled by a programmable US system (Verasonics, Vantage 256, Verasonics Inc., Redmond, WA, USA), that was used for conducting PCD.

A diluted MB solution was injected into the tube phantom. To match the MB concentration to a similar concentration as used in mice models[24], the MB solution was diluted with degassed Dulbecco's phosphate buffered saline (PBS; 02-023-1A, Biological Industries Israel, Beit-Haemek, Israel) to a final concentration of 1.25 x 10^7 [MB/ml]. The function generator was triggered by the Verasonics system and transmitted a single sinusoidal burst of 100 cycles at a center frequency of 250 kHz. During sonication, the PCD array recorded for 1.6 s. This injection-transmit-receive sequence was repeated with different sonication PNPs, and the tube was flushed with PBS between measurements. For controls, the same sequence was performed while PBS was injected instead of diluted MB solution.

PCD data analysis

The acquired RF signals from each transducer element were applied with a fast Fourier transform, and the frequency-domain signals were averaged to enhance the signal-to-noise-ratio. SCD and ICD were extracted according to the method presented in Farny et al.[67] Briefly, a 20 kHz window was defined around each harmonic of the transmission frequency (a harmonic is defined as n x f_0, n = 1,2,3 …). A modified comb filter was applied to eliminate the peaks in these windows and replace them with random samples from the conjugated regions of the spectrum. A high-pass-filter with a cutoff frequency of 1.5 x f_0 was then applied to eliminate the contribution of the transmitted wave. The ICD was defined as the root-mean-square amplitude of the filtered signal. The SCD was calculated as the difference between the root-mean-square of the original signal amplitude and the ICD. Finally, the results of SCD and ICD were normalized by the vessel cross-section to compensate for a possible decrease in MB quantity caused by the liquid volume as in the 100 μm tubes.

In-vivo BBBD

The mice were anesthetized with 1.5% isoflurane using a low flow vaporizer system (50 mL/min, SomnoFlo, Kent Scientific). The mice heads were completely shaved, and US gel was applied. The mice were placed in a supine position on top of an agarose pad, at the focal spot of the FUS setup described in the PCD experiments section. The mice were mechanically aligned using a custom two-axis (X-Y) stereotaxic system that was connected to the water tank (Figure 3A). The focal spot size was 7 mm laterally and 50 mm axially, which is appropriate to conduct BBBD in large brain portions, and mainly in the hypothalamus. BBBD was performed by systemically injecting 2 × 10^7 MB in 50 μL of degassed PBS. Thirty seconds post MB injection, the mice received the FUS treatment consisting of 1 ms bursts at 250 kHz. The total sonication period was 60 s with a PRF of 1 Hz (0.1% duty-cycle). Sonication PNP was optimized to induce safe, mild BBBD, that was visible in fluorescent microscopy, without signs of microhemorrhage in histology. Three PNPs were tested: 150, 175 and 263 kPa. After sonication, the mice were systemically injected with two dyes: 2% Evans Blue dye (EB; E2129, Sigma Aldrich) (4 mL/kg, diluted in PBS), and 6 mg/mL Fluorescein isothiocyanate–Dextran (FITC-Dextran; 52471, Merck, Kenilworth, NJ, USA) (4 mL/kg, diluted in normal saline). Three different EB circulation times were tested: 8, 18, and 28 min, to identify the optimal circulation duration that enabled localized EB detection for each blood vessel (Figure S1). FITC-Dextran circulation time was 10 min to maintain a strong fluorescence signal inside the vessels, without leakage.[42] In between injections, the mice were allowed to wake up for better circulation. Two groups of mice were tested in each experiment: a no treatment control group that was injected with the two dyes but did not receive MB + FUS treatment, and a treated group with MB + FUS and the dyes.

Ten minutes post FITC-Dextran injection, the mice were euthanized. The brains were quickly harvested, covered in tissue freezing medium (Leica OCT cryo compound, Leica Biosystems, Nussloch GmbH, Heidelberger, Germany) and flash-frozen using liquid nitrogen. After flash-freezing, the brains were transferred to a −80°C refrigerator. The freezing procedure was established by comparison to standard Paraformaldehyde (PFA; 50-259-99, Fisher Scientific). Fixation was done by placing the fresh tissue in 4% PFA solution for 24 h, then transferring to 30% sucrose solution up to full precipitation. The brains were washed with PBS, frozen with liquid nitrogen and transferred to −80°C for storage. The PFA preservation resulted in the leaking of the FITC-Dextran outside the vascular system and did not allow for vessel segmentation.

Microscopy imaging

On the day of microscopy imaging, the frozen brains were transferred to a −20°C cryostat microtome (CM1950, Leica Biosystems) and coronally cut to slices of different thicknesses. The sections were placed on standard microscope slides within a closed slide box for air-drying at room temperature for 5–60 min. Three different slice section thicknesses of 12, 20 or 50 μm were tested for the control brains,

to optimize the number of clearly visible blood vessels with a good signal and reduced blurriness that can be a byproduct of out of focus planes (Figure 1). The optimal thickness of 20 μm was selected for the treated brains and the PFA preserved brains. The brain slides were imaged within 1 h of sectioning to avoid further EB perfusion.[42] Images were acquired with a motorized upright fluorescence microscope (BX63, Olympus life science, Waltham, Massachusetts, USA) with an ×20 objective (UPLFLN 20X, Olympus life science). This objective had a focal depth of 1.1 μm. The excitation wavelengths and exposure times were 508 nm and 1150 msec for FITC-Dextran, and 615 nm and 115 msec for EB. All the imaging parameters were consistent for all sections. The final images were 1920 × 1200 pixels in size, with a pixel size of 0.29 μm in the imaging plane.

Image processing

Microscopy image processing was performed using MATLAB. Preprocessing included the splitting of all images into two channels: the green channel that marked the blood vessels with FITC-Dextran and the red channel that showed EB extravasation from the blood stream into the surrounding perivascular area. Post processing was then applied as follows. The first step utilized the green channel to perform blood-vessel segmentation and characterization. This was carried out using a modified version of the Rapid Editable Analysis of Vessel Elements Routine (REAVER) tool,[68] that was adjusted specifically for this task. Segmentation yielded a binary mask of all vessels in the frame, from which the vascular skeleton was extracted (Figure 5D). Branchpoint localization was used to separate the vascular network into individual vessels, which were then used for BBB leakage quantification.

The second step was to calculate the single vessel median radius as described by Corliss et al.[68] Briefly, for each point on the vessel centerline, the distance to the closest point outside the vessel was calculated. This distance represented the local vessel radius. The median of all local radii of the vessel was calculated. Two other network morphology features were extracted for each frame: the bifurcation density and the length density. The bifurcation density was calculated as the number of bifurcations in the vascular skeleton divided by the frame area, and the length density was calculated as the total length of the vessels divided by the frame area.

After obtaining the morphological features of the blood vessels, the following steps were carried to quantify EB extravasation and BBBD for each blood vessel. In the third step, the binary mask obtained from the green channel was applied to the red channel. By doing so, the interior of each blood vessel was removed from the frame, leaving behind a frame with the EB intensity in the perivascular area (Figure 5E). This step served to remove the blood vessel content itself and focus on the EB extravasation.

In the fourth step, the size of the perivascular area around the blood vessels was determined. This area was defined by two user specified constants: the initial distance from the vessel wall (W_i) which was used to eliminate segmentation-related errors, and the perivascular area width (d). Then, individual blood vessels were extracted from each image by subtracting the entire vascular mask from the single-vessel perivascular area mask. This was done to make sure that the perivascular area did not include nearby vessels.

In the final step, the EB channel intensity was rescaled to a range of [0,1] and the median pixel intensity in the perivascular area (defined in the previous steps) was calculated. Steps 3–5 were repeated for each blood vessel in each frame.

Hematoxylin & Eosin staining

The safety of the BBBD treatments was assessed with standard Hematoxylin (3801542, Leica Biosystems) and Eosin (3801602, Leica Biosystems) staining of the sliced brain sections. The stained slides were imaged using the brightfield channel of the same microscope as for fluorescence imaging.

QUANTIFICATION AND STATISTICAL ANALYSIS

Quantitative analysis

Vascular morphology in different regions of the brain (hippocampus, hypothalamus, striatum, and thalamus) for the control and MB + FUS treated groups was evaluated by quantification of length and bifurcation density (Figures 6C and 6D). The microvasculature diameter distribution was calculated and plotted as a diameter histogram (Figures 6A and 6B). Because the majority of the blood vessels in the mouse brains

were smaller than 10 μm (average diameter was 4.98 ± 1.9 μm), we chose to focus on blood vessels that are below 10 μm, and exclude vessels with unclear borderlines.

In the second stage, EB quantification was performed for individual blood vessels, where in bifurcating vessels the segments before and after the bifurcation were considered two separate blood vessels. Different perivascular areas were compared. Three initial distances from the blood vessel wall, W_i, of 0, 2 and 5 pixels (corresponding to 0, 0.59 and 1.46 μm), and three different perivascular widths, d, of 1, 5, and 10 pixels (0.29, 1.46 and 2.93 μm). For each combination of hyperparameters, the EB intensity results were divided into groups based on the vessel diameter. Vessels with diameters of 2–10 μm were sorted into diameter groups at 1 μm intervals (2–3, 3–4, …,9–10 μm). The EB intensity in the perivascular area was calculated for each blood vessel in each diameter group, for the control and treated brains, and plotted as EB intensity histograms (Figures 7B and 7C), and as a comparison to other diameters (Figures 7D and 7E). Note that each frame contained blood vessels with different orientations, ranging from circular cross sections when the blood vessels were perpendicular to the image plane, to lines when they were parallel to the imaged plane. To reduce segmentation noise in the small capillaries (<4 μm), blood vessels with a minimal length of less than 10 μm were removed. The number of capillaries that were used for the analysis was 1075.

Finally, the percentage of BBBD blood vessels for each diameter group was assessed by setting a threshold that was determined based on the EB intensity of the control group for each diameter. The threshold was two standard deviations above the mean control EB intensity. In the treated group, and for each diameter, all the blood vessels whose EB intensity exceeded the corresponding threshold were considered a strong BBBD (Figure 7E). This analysis was conducted for each frame and vessel diameter. Comparisons were carried out between frames.

Statistics

Statistical analysis was performed using MATLAB and GraphPad Prism. The results are presented as the mean ± SD. Statistical tests are reported in the captions. p values of less than 0.05 were considered significant and were adjusted for multiple comparisons as indicated in the captions.

ADDITIONAL RESOURCES

All the code used for image processing and analysis can also be found in the following GitHub repository: https://github.com/TheIlovitshLab/BBBD-REAVER.